# Mechanisms of THz generation from silver nanoparticle and nanohole arrays illuminated by 100 fs pulses of infrared light

D. K. Polyushkin,[1,2,*] I. Márton,[3,4] P. Rácz,[3] P. Dombi,[3,5] E. Hendry,[1] and W. L. Barnes[1,6]

[1]*School of Physics and Astronomy, University of Exeter, Stocker Road, Exeter EX4 4QL, United Kingdom*

[2]*Institute of Photonics, Vienna University of Technology, Gusshausstrasse 27-29, 1040 Vienna, Austria*

[3]*Wigner Research Centre for Physics, H-1121 Budapest, Konkoly-Thege M. út 29-33, Hungary*

[4]*Department of Experimental Physics, University of Pécs, H-7624 Pécs, Hungary*

[5]*Max-Planck-Institut für Quantenoptik, 85748 Garching, Germany*

[6]*Complex Photonic Systems (COPS), MESA+ Institute for Nanotechnology, University of Twente, 7500 AE Enschede, The Netherlands*

(Received 6 November 2013; revised manuscript received 12 February 2014; published 24 March 2014)

We study THz pulses generated from plasmonic metal nanostructures under femtosecond illumination of near-IR light. We find two regimes of excitation, according to the order of the dependence of the THz fluence on the incident near-IR intensity: less then second order at low intensities, changing to approximately fourth order for higher intensities. These regimes are most likely associated with two THz generation mechanisms: optical rectification, and the ponderomotive acceleration of ejected electrons. These data provide evidence that both mechanisms can be at work in the same experiment.

DOI: 10.1103/PhysRevB.89.125426 PACS number(s): 78.67.Bf, 42.65.Ky, 42.65.Re, 73.20.Mf

## I. INTRODUCTION

The development of free-electron lasers [1,2], quantum-cascade lasers [3], and tabletop spectrometers based on ultrafast laser pulses [4] has opened up the THz spectrum for scientific and technological exploration. THz radiation produced by illumination of a variety of materials by short pulses of laser light has been shown to arise from a number of mechanisms including optical rectification (OR) in nonlinear dielectric materials [5], photoexcited plasmas in gases [6], demagnetization in ferromagnets [7], and from surface field emission and photo-Dember effects in semiconductors [8,9].

In recent years, there have been a number of experiments in which THz emission has been observed when metallic surfaces and nanostructures have been illuminated by ultrafast IR laser pulses. Experiments on THz generation from optically thin metal surfaces were reported in 2004 [10]. Since then different metallic materials and structures have been used to generate THz radiation: nanostructured silver and gold films [11–13], semicontinuous metal films [14,15], and metallic nanoparticles [15,16]. Two distinct mechanisms have been proposed to explain the observed generation of THz radiation: OR on metal surfaces [10,14,16–18] and multiphoton photoelectron emission (MPE) [11,15,19,20]. In the latter case, the THz radiation is produced by the ponderomotive acceleration of the ejected electrons caused by the high electric field gradients that occur in the proximity of metal surfaces [21], owing to plasmonic enhancement [11,15].

The present situation is somewhat confusing because frequently the conditions pertinent to many of the experiments for which OR is proposed as the THz generation mechanism are significantly different from those for which ponderomotive acceleration is invoked. As Ramakrishnan *et al*. recently pointed out [18], the different observed dependencies of the THz fluence on pump power do not necessarily contradict each other, rather they may be associated with different regimes of THz emission that occur under these different experimental conditions. Experiments for which OR is invoked typically involve relatively low peak-power Ti:sapphire laser pulses (see Refs. [14,16,18]). The high repetition rate of these laser sources enables lock-in detection techniques that are well suited to the retrieval of relatively weak signals from second-order nonlinear processes such as OR. For such systems, the low incident pulse intensities (typically in the range 6–25 MW cm$^{-2}$, $3 \times 10^{-4}$–$1.2 \times 10^{-3}$ mJ cm$^{-2}$ per pulse [14]) make the observation of high-order nonlinearities difficult. The much higher peak power typical of amplified Ti:sapphire lasers (typically in the range 2.5–40 GW cm$^{-2}$, 0.25–4 mJ cm$^{-2}$ per pulse [19]) makes the observation of higher-order nonlinear processes more likely. However, the distinction outlined above is not clear-cut; we note that Kadlec *et al*. (Refs. [10,17]) have previously explained their results, measured using an amplified laser system, by invoking only OR.

In this article we elucidate this apparent inconsistency by presenting results from samples that show both OR and MPE in the same experimental arrangement. For a periodic arrangement of holes in a silver film, we find THz emission to be dominated by OR for low incident intensities, while at higher incident energies MPE takes over. An array of small metallic particles, on the other hand, displays only MPE under the illumination conditions used in our experiments. This indicates that sample morphology, and in particular the strength of the local electromagnetic enhancement, is a critical factor in determining the dominant emission mechanism, thereby demonstrating a clear correlation between plasmon coupling and the THz signal.

In our previous work [15] we looked at the THz emission from arrays of metallic nanoparticles. We made use of the plasmon modes supported by the metallic nanoparticles by ensuring that the incident pulses were at a frequency that matched that of the plasmon modes. In this way the strength of the optical electric field in the vicinity of the particles is

*Corresponding author: dmitry.polyushkin@tuwien.ac.at

 

enhanced, strengthening the effectiveness of the THz emission process. We showed that the THz emission of such samples is broadly consistent with a model based upon MPE. At the lowest incident pulse energies used, no indication of lower-order process, such as OR, were observed. Reducing the pump intensities further, the obvious approach if one is seeking any lower-order processes, was not possible due to limitations imposed by the noise floor of the experimental setup. An alternative is to design a sample in which the higher-order, MPE processes are diminished with respect to the lower-order OR processes. One key parameter here is the local field enhancement: For samples which exhibit strong local enhancement, higher-order processes will be more likely, while the converse is true for low field enhancement. A simple array of nanoholes typically exhibits lower resonant field enhancements than the complimentary particle array [22,23]; this is the structure we choose to compare in experiment.

## II. SAMPLE FABRICATION

To fabricate the structures we used nanosphere lithography (NSL) [24,25], a technique that enables the fabrication of large areas ($\sim$1 cm$^2$) of ordered nanostructures. The standard NSL technique [25] enabled us to produce nanoparticle arrays; the nanohole arrays were fabricated using a modified NSL technique [26,27]. Sample fabrication comprised the following steps. A clean glass substrate was immersed in de-ionized water. A suspension of colloidal polystyrene nanospheres was then introduced onto the water surface. The spheres self-assemble into a hexagonal close-packed monolayer array and this layer of nanospheres was then transferred onto the glass substrate. As the water evaporates the monolayer array of nanospheres remains. This array of spheres is then used as a template through which to evaporate metal. Once the spheres are removed, typically by ultrasonication in toluene, a honeycomb array of triangular metal nanoparticles is left behind. To produce nanohole arrays an extra step is introduced before metal evaporation. The assembled spheres are etched using an oxygen plasma reactive-ion etch, which allows for a controllable size reduction of the polystyrene spheres. Once etching has been carried out metal is evaporated through the resulting mask and the spheres are then removed.

Scanning electron micrographs (SEMs) of typical nanoparticle and nanohole arrays produced in this way are shown in Fig. 1. The arrays used here were fabricated using polystyrene spheres with a diameter of 780 nm; the thickness of the evaporated silver film was 50 nm. The fractional coverage of the surface by metal is $\sim$27% for the hole array, and $\sim$8% for the particle array [see insets of Figs. 1(a) and 1(b)]: This gives rise to an amplifying factor for the observation of weak OR signals in the hole array, as we see below. To characterize the samples we measured optical transmittance spectra of our nanoparticle and nanohole arrays, as shown in Figs. 1(a) and 1(b), respectively.

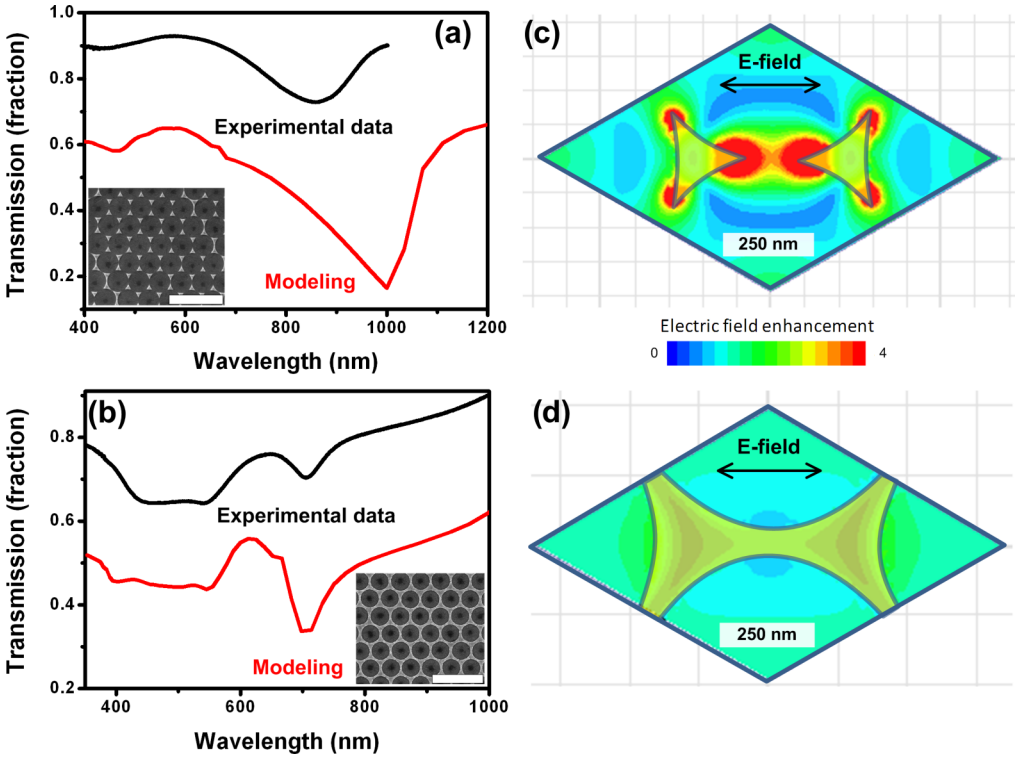


FIG. 1. (Color online) Optical transmittance spectra of the silver nanoarray structures. Experimental data (black) and modeling (red) for particles (a) and holes (b). The difference in transmittance levels between experiment and theory may be due to sample inhomogeneity (regions of sample with no metal). The inset for each shows an SEM of a representative sample, the scale bars in the insets are 2 $\mu$m. Field distribution around (c) particles and (d) holes calculated using finite-element modeling. Incident light with a wavelength 1000 nm is normal to the substrates. The plots show the time-averaged magnitude of the electric fields. For the particles (c) the regions of highest field are at the tips of the particles. For the holes (d) the regions of highest field are over the metal regions.

### III. NUMERICAL MODELING

For comparison the transmittance spectra calculated using a finite-element model are also shown. We performed numerical simulations of the electromagnetic fields in the vicinity of the nanoparticles using a commercial finite-element package (Ansoft HFSS version 11.0) with a mesh size of approximately 5.0 nm. Permittivity values for gold and for the glass substrate were taken from [28]. The incident field was taken to be linearly polarized; the direction is indicated in Fig. 4. Due to the symmetry of the hexagonal structure, this choice did not affect the calculated spectrum. Periodic boundary conditions were used to minimize the spatial extent of the model, and absorbing boundary conditions in the incident and transmission regions were placed 800 nm from the substrate interface. We then calculated transmittance spectra by integrating the power density on the transmission absorbing boundary and normalized to the incident field.

The rather complex spectra are typical of those obtained from such arrays [27]. The dip in transmittance at ∼840 nm (∼1000 nm) and at ∼710 nm (∼700 nm) in the experimental (modeled) data for particle [Fig. 1(a)] and hole [Fig. 1(b)] arrays, respectively, is indicative of the main plasmon resonance associated with these arrays. The difference in the resonance wavelength between the experimental data and the model is most likely due to a mismatch between the model and the experiment regarding the exact size and aspect ratio of the particles. In Figs. 1(c) and 1(d) we show the calculated field distributions associated with the plasmon modes supported by the nanoparticle and nanohole structures, calculated on resonance. From these data we find that the maximum field enhancement for particles and holes differs by an order of magnitude (note they are plotted on the same linear scale to highlight this difference). The field enhancement for hole arrays is ∼2 while that for particles is ∼10–20, as expected [23].

### IV. THz EXPERIMENTS

The generation and detection of THz radiation was performed by electro-optical sampling using 100 fs laser pulses with a central wavelength of 800 nm from an amplified Ti:sapphire laser in standard THz-TDS setup [15]. The incident light was focused down to a 1.5-mm-diameter beam having a maximum intensity of about 200 GW cm$^{-2}$. The laser beam was split into two beams, one illuminating the sample, the other going to a 1-mm-thick ZnTe 110-oriented electro-optical crystal used for the detection of the generated THz pulses. Since the THz pulses are significantly longer than the laser pulses (several ps compared to 100 fs), the THz field can be approximated as a static field that biases the detection crystal. The THz field induces birefringence in the crystal, and this induced birefringence modifies the polarization state of the 800 nm detection pulse that is coincident with the THz pulse on the crystal. The change in polarization state is measured using a polarizing beam splitter and a pair of balanced photodiodes. By varying the delay between THz and probe pulses the temporal profile of the detected THz field can be obtained.

### V. THz EMISSION RESULTS

To measure the dependencies of the generated THz fluences as a function of the incident intensity we employed neutral density filters to vary the optical power over nearly three orders of magnitude, from 0.3 to 200 GW cm$^{-2}$. The sampling technique allowed us to measure the transient THz field. The time-domain signal recorded in this way was then used to retrieve the radiation spectrum by means of a Fourier transform [Fig. 2(a)]. The THz fluence was determined by integrating the square of the measured spectrum in the range of frequencies from 0 to 3 THz [Fig. 2(b)]. The THz data shown in Fig. 2 were obtained from the samples when illuminated at a polar angle of ∼50°. We avoided normal incidence illumination since, for the centrosymmetric nature of our arrays, electron currents in the plane will cancel out over the duration of the incident pulse. THz generation at non-normal incidence can be achieved by an appropriate choice of noncentrosymmetric structure [29].

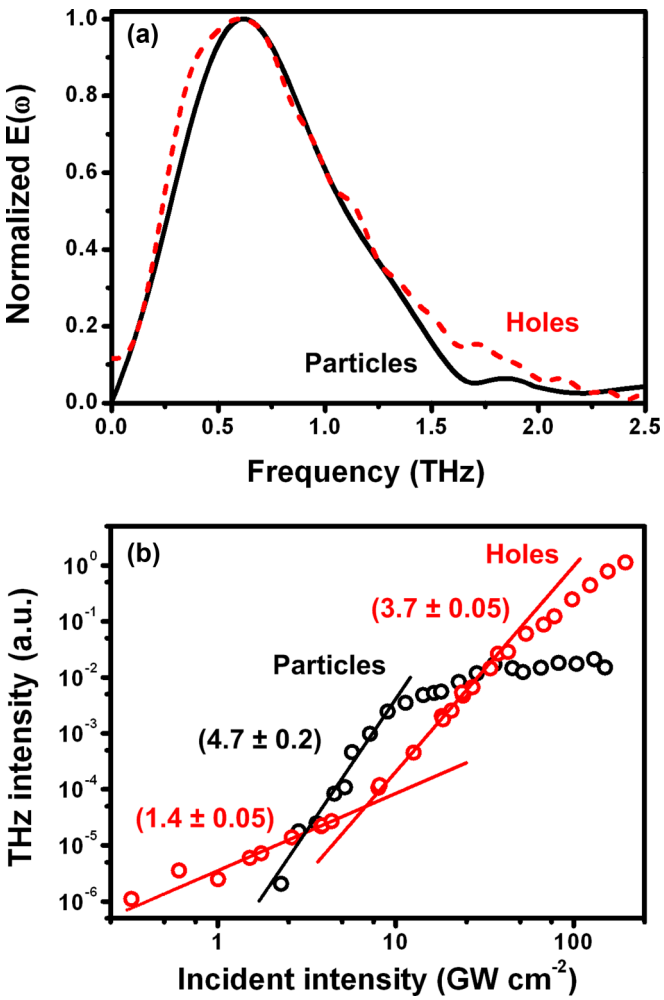


FIG. 2. (Color online) THz emission data. Representative spectra of the emitted THz radiation for particle (black solid line) and hole (red dashed line) arrays are shown in (a). Measured THz fluence as a function of incident optical intensity for the arrays of nanoparticles and nanoholes made by NSL technique are shown in (b), where the numbers in the brackets are the fitted orders of the appropriate sections of the data.

The measured THz fluence as a function of incident intensity is plotted in Fig. 2 for both particle and hole arrays. For particle arrays the data (black) show two distinct regions. For incident intensities below $\sim$10 GW cm$^{-2}$ there is a 4.7 $\pm$ 0.2 order dependence, indicative of MPE [15]. For incident intensities above $\sim$10 GW cm$^{-2}$ the data show a much reduced power dependence; this is most likely associated with the onset of tunnel ionization of nanoparticle samples at these intensities [15]. For the lowest pump intensities, set by the signal-to-noise level in the experiment, there is no indication of a transition to the lower power dependence expected for OR. In contrast, the data from the hole arrays show three different regions. For intermediate incident intensities, between $\sim$5 and $\sim$50 GW cm$^{-2}$, the data show a 3.7 $\pm$ 0.05 order dependence of the THz fluence on the incident optical intensity. Again, this higher-order dependency is suggestive of MPE [15]. This order is slightly lower than the result for the particles, an effect that most likely results from a rapid onset of the same saturation effects for high incident energies described above. Indeed, above $\sim$50 GW cm$^{-2}$ the THz fluence starts to saturate in a way that is similar to that which we observed for particles [15]. However, an interesting aspect is revealed in these data for incident intensities below $\sim$5 GW cm$^{-2}$, where a clear transition to a low, less than second-order dependence, is observed. Such low-order dependence is completely inconsistent with MPE but is more consistent with OR. Note that we expect the transitions between the different regimes of operation will not occur at the same incident intensities for the two array types since the strength of the electric field will depend on the extent of the plasmonic enhancement.

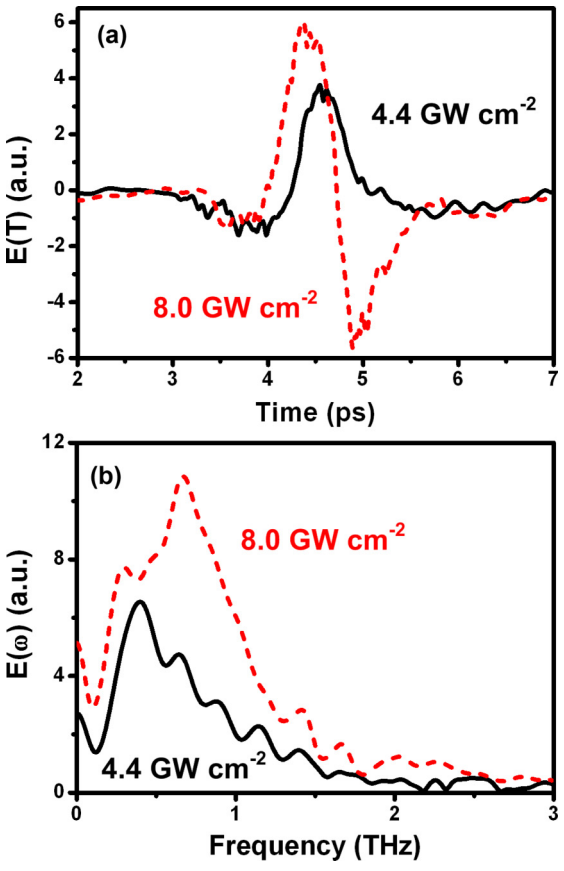


FIG. 3. (Color online) The data taken from the nanohole array at incident intensities of 4.4 GW cm$^2$ (black, solid line) and 8.0 GW cm$^2$ (red, dashed line). The time-domain signals are shown in (a), and the spectra of THz pulses are shown in (b). Small oscillations in the spectra at frequencies above 0.5 THz are probably due to noise in the time-domain signal.

The ratio of the transition intensities between the regimes of MPE and tunnel ionization for nanoholes and nanoparticles is about a factor of 5 [see Fig. 2(b)]. One expects the transition intensity to be inversely proportional to the second power of the field enhancement (Eq. S3 in the supplemental material of [15]). Taking into account the maximum values of the field enhancement from Fig. 1 more than an order of magnitude difference between the transition intensities for holes and particles might be expected. However, one should note that this estimation is oversimplified, since the field in the vicinity of the structures is very inhomogeneous.

Interestingly we also observe a transition between the mechanisms of generation in the spectra of the THz pulses, which undergo a significant change at an incident intensity of $\sim$5 GW cm$^{-2}$. The shape of the time-domain signal from the nanoholes changes when the incident intensity increases above this value [Fig. 3(a)]. In conjunction with this change in the slope of the time-domain signal, there is also a change in the spectrum of the THz radiation [Fig. 3(b)]; a second peak appears at higher frequency. This observation is specific to the nanohole array; for nanoparticle arrays the THz pulse spectrum and the shape of the time-domain signal varies only slightly over the whole range of incident intensities used in the experiment.

To investigate this effect in detail we plotted the time-domain signals and the THz radiation spectra for a range of incident intensities from 4.4 to 64.2 GW cm$^{-2}$ (Fig. 4). From the data shown in Fig. 4(a) it can be seen that the signal shape abruptly changes when the intensity is increased from 4.4 to 8.0 GW cm$^{-2}$. In particular, the second minimum (negative peak) becomes much more distinctive. With further increase in incident intensity, the shape of the signal continues to change, but much more gradually. The ratio of the magnitude of the main (positive) and second (negative) peaks changes with a higher amplitude of the positive peak at low incident intensities turning into a higher amplitude of the negative peak at higher pump energies. The continuous transformation of the time-domain signal with incident intensity leads to signals at the lowest (4.4 GW cm$^{-2}$) and the highest (64.2 GW cm$^{-2}$) intensities looking as though they have reversed phases (all the parameters of lock-in detection were the same during the data acquisition). To show this effect more clearly, we plotted these normalized signals on one plot with a reversed phase of the second signal [Fig. 5(a)].

On increasing the incident intensity the THz spectra also change. The spectrum abruptly changes when the intensity increases from 4.4 to 8.0 GW cm$^{-2}$, namely, the spectral maxima shift from 0.4 THz at lower intensity to 0.65 THz at higher pulse energies. With a further increase of the pump power both maxima in the spectrum develop, giving a single peak at moderate incident intensities, 20–40 GW cm$^{-2}$. At the highest intensity (64.2 GW cm$^{-2}$) these two peaks (occurring at frequencies 0.4 and 0.65 THz) appear distinct again. The

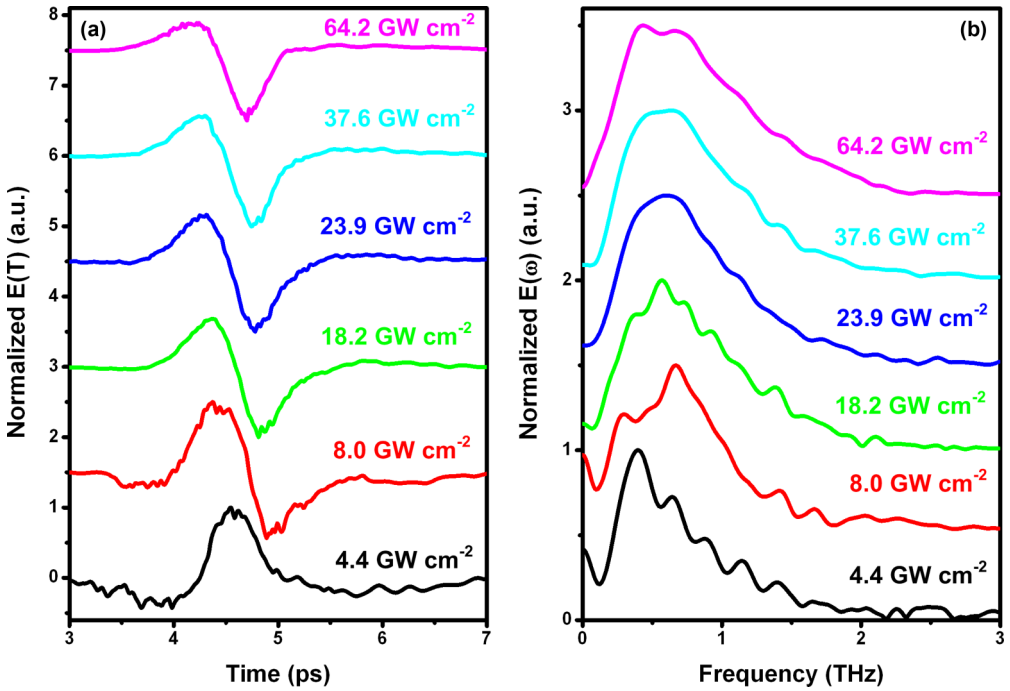


FIG. 4. (Color online) Evolution of (a) time- and (b) frequency-domain signals acquired from the nanohole array at incident intensities of 4.4, 8.0, 18.2, 23.9, 37.6, and 64.2 GW cm$^{-2}$. The signals are normalized and upshifted for comparison's sake.

frequency peaks coincide with those obtained at intensities 4.4 and 8.0 GW cm$^{-2}$ [Fig. 5(b)].

Such signal and spectral evolution, with an abrupt change at the incident intensity where the transition between the order dependences occurs, most probably indicates a shift between different regimes of THz generation. However, further investigation of this effect is required to understand these phenomena better.

## VI. ELECTRON EMISSION RESULTS

To gain further insight into the physical origin of the THz emission we used a time-of-flight electron spectrometer to measure the spectra of electrons generated following illumination with femtosecond laser pulses using a system similar to that in [30]. A representative electron emission spectrum acquired at an incident optical intensity of ∼60 GW cm$^{-2}$ is shown in Fig. 6(a) for both types of array. Electrons with kinetic energies up to ∼40 eV are observed. These energies are much higher than the photon energy, 1.55 eV, indicating the ponderomotive electron acceleration mechanism [30,31]. A cutoff electron energy is apparent in these data at ∼20–40 eV; this cutoff energy scales linearly with the incident intensity for low incident pulse intensities, which also points towards a mechanism involving ponderomotive electron acceleration (see [30,31] as well as supporting info for [15]). The integrated photocurrent as a function of incident intensity for both array types is shown in Fig. 6(b). These experimental data are in good agreement with previously published results on electron emission from silver films [31] and nanoparticles [30]. Fitting power functions to the data, we obtain a 4.0 ± 0.4 order dependence for incident intensities in the range ∼25 to ∼55 GW cm$^{-2}$ for the hole array. Above this incident intensity the order decreases. For incident intensities below ∼55 GW cm$^{-2}$ the order of the process corresponds to a number of photons required to liberate a single electron (1.55 eV photons, silver work function ∼4.6 eV [32]). For higher incident intensities the experimental data for both particles and holes show a lower-order dependence, often attributed to electrons tunneling through a tilted vacuum potential (e.g., see [31,33], and references therein). Similar behavior is observed for the particle arrays, but with the transition shifted to lower intensities, similar to the effect observed in the THz emission data in Fig. 2.

## VII. DISCUSSION

Comparing Figs. 2(b) and 6(b), we see many similarities between the intensity dependences of the THz emission and the photoelectron emission. Most obvious is the correlation in the ranges of high-order intensity dependence (approximately fourth and fifth order for THz emission for particles and holes, respectively, and approximately fourth order for electron emission from both structures). This suggests that the pulsed photoemission of electrons gives rise to the time-varying current density $J(t)$ responsible for the radiated THz pulse. However, as one expects the electric field of the emitted THz pulse to follow $dJ/dt$, one might expect the THz intensity to exhibit a higher-order dependence on the incident intensity than is observed for the photocurrent, while in experiment they are comparable. It is likely that, as with OR (see below), other processes are simultaneously at work which diminish the intensity dependence of the emitted THz intensity. For example, the high field amplitude gradient in the vicinity of the nanostructures may have an influence on ponderomotive

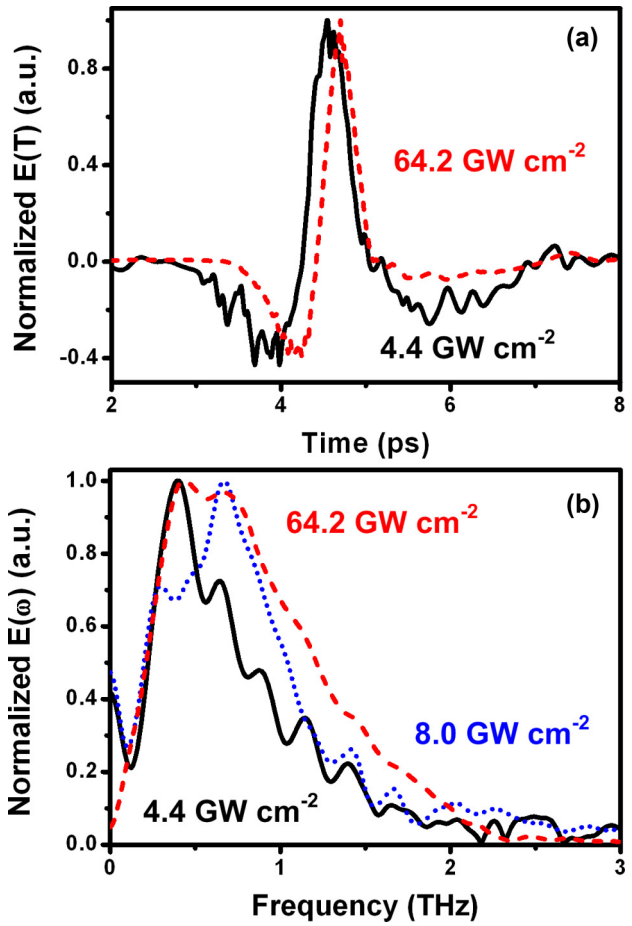


FIG. 5. (Color online) THz emission data taken from the nanohole array. (a) Time-domain signal obtained at incident intensities of 4.4 GW cm$^2$ (black, solid line) and 64.2 GW cm$^2$ (red, dashed line). (b) Spectra of THz pulses generated at incident intensities of 4.4 GW cm$^2$ (black, solid line), 8.0 GW cm$^2$ (blue, dotted line), and 64.2 GW cm$^2$ (red, dashed line). The data are normalized and in addition, the phase of the signal in (a) taken at intensity 64.2 GW cm$^2$ is reversed.

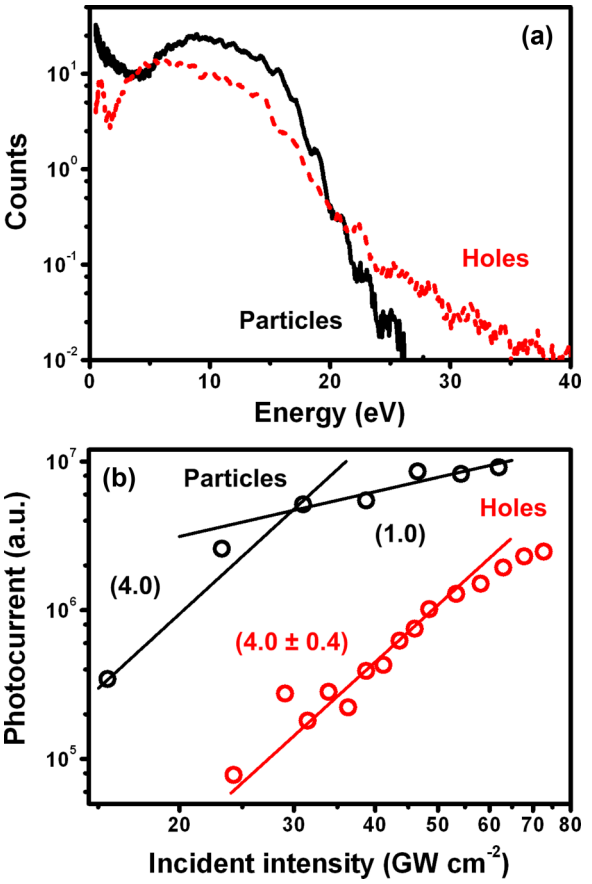


FIG. 6. (Color online) Electron emission data. Representative electron energy spectra for electrons collected from particle (black solid line) and hole (red dashed line) arrays are shown in (a), obtained at incident optical intensity ~60 GW cm$^{-2}$. Electron count rate as a function of incident optical intensity for arrays of nanoparticles (black) and nanoholes (red) made by NSL technique are shown in (b). The numbers in brackets are the fitted orders of the processes.

acceleration [34,35], while electron emission by tunneling will also give rise to a lower order.

The intensity dependence of the hole array THz emission presented in Fig. 2(b), meanwhile, exhibits a much lower-order dependence of 1.5 ± 0.2 (when averaged over several samples) for incident intensities <10 GW cm$^{-2}$. It is clear that the mechanism of THz emission in this region has nothing to do with MPE, and is most likely the result of OR. For OR one might expect a second-order dependence. For OR a strict second-order dependence is usually only observed for very low incident intensities, as processes such as two-photon absorption lead to a lower-order dependence as the incident intensity is increased [36].

It is interesting to note that the intensity dependences shown in Fig. 2(b) are one of the few ways to distinguish higher-order processes such as MPE and lower-order processes such as OR. The THz pulse emitted during both processes will exhibit an electric field that follows $dJ/dt$, in the far field. With a finite length of excitation pulse and a finite plasmon lifetime, $J$ will exhibit an amplitude function given by the excitation and decay lifetimes. However, one should note that this by itself is not enough to generate a pulse of low-frequency THz radiation: one must also break mirror symmetry so that $J$ has a preferred direction, with local current moving more easily in one particular direction. This symmetry breaking is required for both MPE and OR mechanisms, with the symmetry breaking occurring in our samples at the interface, with the relevant current component perpendicular to the interface. It is therefore difficult to use symmetry and emission patterns to distinguish these mechanisms.

In summary, for THz pulses generated from plasmonic metal nanostructures under femtosecond illumination of near-IR light we find two regimes of excitation, according to the order of the dependence of the THz fluence on the incident near-IR intensity. An observed less than second-order dependence for low incident intensities onto a metallic hole array is most likely associated with optical rectification. An approximately fourth- to fifth-order dependence observed for higher intensities onto both metallic hole and particle arrays is

most likely associated with the ponderomotive acceleration of photoejected electrons. This result is further corroborated by results of electron emission measurements on similar samples, which provide evidence of the link between electron emission and THz generation for this high-intensity regime. These data provide evidence that THz generation by both optical rectification and multiphoton photoemission may occur in the same experiment.

## ACKNOWLEDGMENTS

This work was supported by the Hungarian Scientific Research Fund (Projects 81364 and 109257). P.D. acknowledges support from the Bolyai Fellowship, P.R. from the Postdoctoral Fellowship of the Hungarian Academy of Sciences. P.D. was also supported by a Marie Curie Fellowship of the EU (project acronym "UPNEX").

[1] G. L. Carr, M. C. Martin, W. R. McKinney, K. Jordan, G. R. Neil, and G. P. Williams, Nature **420**, 153 (2002).
[2] G. P. Williams, Rep. Prog. Phys. **69**, 301 (2006).
[3] R. Köhler, A. Tredicucci, and F. Beltram, Nature **417**, 156 (2002).
[4] K. Sakai, in *Terahertz Optoelectronics* (Springer, Berlin, 2005), p. 350.
[5] J. Shan, A. Nahata, and T. F. Heinz, J. Nonlinear Opt. Phys. Mater. **11**, 31 (2002).
[6] Y. Chen, M. Yamaguchi, M. Wang, and X.-C. Zhang, Appl. Phys. Lett. **91**, 251116 (2007).
[7] E. Beaurepaire, G. M. Turner, S. M. Harrel, M. C. Beard, J.-Y. Bigot, and C. A. Schmuttenmaer, Appl. Phys. Lett. **84**, 3465 (2004).
[8] A. Reklaitis, J. Appl. Phys. **109**, 083108 (2011).
[9] M. B. Johnston, D. M. Whittaker, A. Corchia, A. G. Davies, and E. H. Linfield, Phys. Rev. B **65**, 165301 (2002).
[10] F. Kadlec, P. Kuzel, and J. L. Coutaz, Opt. Lett. **29**, 2674 (2004).
[11] G. H. Welsh and K. Wynne, Opt. Express **17**, 2470 (2009).
[12] F. Garwe, A. Schmidt, G. Zieger, T. May, K. Wynne, U. Hubner, M. Zeisberger, W. Paa, H. Stafast, and H. G. Meyer, Appl. Phys. B: Lasers Opt. **102**, 551 (2011).
[13] A. Schmidt, F. Garwe, U. Hübner, T. May, W. Paa, M. Zeisberger, G. Zieger, and H. Stafast, Appl. Phys. B **109**, 631 (2012).
[14] G. Ramakrishnan and P. C. M. Planken, Opt. Lett. **36**, 2572 (2011).
[15] D. K. Polyushkin, E. Hendry, E. K. Stone, and W. L. Barnes, Nano Lett. **11**, 4718 (2011).
[16] K. Kajikawa, Y. Nagai, Y. Uchiho, G. Ramakrishnan, and N. Kumar, Opt. Lett. **37**, 4053 (2012).
[17] F. Kadlec, P. Kuzel, and J. L. Coutaz, Opt. Lett. **30**, 1402 (2005).
[18] G. Ramakrishnan, N. Kumar, P. C. M. Planken, D. Tanaka, and K. Kotaro, Opt. Express **20**, 4067 (2012).
[19] G. H. Welsh, N. T. Hunt, and K. Wynne, Phys. Rev. Lett. **98**, 026803 (2007).
[20] Y. H. Gao, M. K. Chen, C. E. Yang, Y. C. Chang, S. Yin, R. Q. Hui, P. Ruffin, C. Brantley, E. Edwards, and C. Luo, J. Appl. Phys. **106**, 7 (2009).
[21] C. M. Aikens, L. R. Madison, and G. C. Schatz, Nat. Photon. **7**, 508 (2013).
[22] T. W. Ebbesen, H. J. Lezec, H. F. Ghaemi, T. Thio, and P. A. Wolff, Nature **391**, 667 (1998).
[23] J. Parsons, E. Hendry, C. P. Burrows, B. Auguie, J. R. Sambles, and W. L. Barnes, Phys. Rev. B **79**, 073412 (2009).
[24] U. C. Fischer and H. P. Zingsheim, J. Vac. Sci. Technol. **19**, 881 (1981).
[25] J. C. Hulteen and R. P. Van Duyne, J. Vac. Sci. Technol. A **13**, 1553 (1995).
[26] C. Haginoya, M. Ishibashi, and K. Koike, Appl. Phys. Lett. **71**, 2934 (1997).
[27] W. A. Murray, S. Astilean, and W. L. Barnes, Phys. Rev. B **69**, 165407 (2004).
[28] E. D. Palik, in *Handbook of Optical Constants of Solids* (Academic Press, New York, 1985), p. 804.
[29] L. Luo, I. Chatzakis, J. Wang, F. B. P. Niesler, M. Wegener, T. Koschny, and C. M. Soukoulis, Nat. Commun. **5**, 1 (2014).
[30] P. Dombi, A. Hörl, P. Rácz, I. Márton, A. Trügler, J. R. Krenn, and U. Hohenester, Nano Lett. **13**, 674 (2013).
[31] P. Dombi, S. E. Irvine, P. Rácz, M. Lenner, N. Kroo, G. Farkas, A. Mitrofanov, A. Baltuska, T. Fuji, F. Krausz, and A. Y. Elezzabi, Opt. Express **18**, 24206 (2010).
[32] A. W. Dweydari and C. H. B. Mee, Phys. Status Solidi A **27**, 223 (1975).
[33] S. E. Irvine and A. Y. Elezzabi, Appl. Phys. Lett. **86**, 264102 (2005).
[34] P. Rácz and P. Dombi, Phys. Rev. A **84**, 063844 (2011).
[35] P. Rácz, S. E. Irvine, M. Lenner, A. Mitrofanov, A. Baltuska, A. Y. Elezzabi, and P. Dombi, Appl. Phys. Lett. **98**, 111116 (2011).
[36] S. Vidal, J. Degert, M. Tondusson, J. Oberlé, and E. Freysz, Appl. Phys. Lett. **98**, 191103 (2011).